1 **Supporting information for**

2 **Amorphous manganese silicate/PVDF membrane in the diffusive gradient in thin-film for**

3 **selective monitoring of lead**

4 Na Huang [a,1], Yating Wang [b,1], Chenxue Ling [a], Xin Liu [a], Yuling Cai [a], Min Deng [c], Chen Chao [a],

5 Gang Yang [a], Lulu Long [a,*]

6

7 a Institute of Ecological and Environmental Sciences, Sichuan Agricultural University, Chengdu,

8 611130, China.

9 b Chengdu Academy of Environment Sciences, Fanglin Road, Chengdu, 610072

10 c Institute of Multipurpose Utilization of Mineral Resources, Chinese Academy of Geological

11 Sciences, Chengdu, 610041, China

12

13 [1] These authors contributed equally to this work.

14 *Corresponding author:

15 E-mail address: lululong@sicau.edu.cn

16

17 **Number of pages: 14**

18 **Number of Texts: 5**

19 **Number of Figures: 9**

20 **Number of Tables: 5**

Experimental Section

Chemicals

Sodium silicate hexahydrate ($Na_2SiO_3 \bullet 9H_2O$), Lead nitrate ($Pb(NO_3)_2$), and Sodium nitrate were purchased from Ke Long Chemical Reagent Co., Ltd., Chengdu, China. Nitrogen, nitrogen dimethylformamide, polyvinylpyrrolidone (PVP K30) were purchased from Sinopharm Chemical Reagent Co., Ltd. In addition, Polyvinylidene fluoride (PVDF) and Manganese chloride tetrahydrate ($MnCl_2 \bullet 4H_2O$) were obtained from Shanghai Aladdin Biochemical Technology Co., Ltd. The DGT devices used in this study were derived from *EasySensor Ltd*. High purity doubly deionized water (Milli-Q water with 18.2 MΩ cm resistivity, Millipore)) was applied to prepare all stock solutions. NaOH and HNO_3 were used to adjust the pH of the solution.

MnSi/PVDF membrane preparation.

A PVDF-supported MnSi bonded phase membrane (referred to as PMn membrane) was prepared by a simple phase invasion technique [1, 2]. Amorphous manganese silicate (MnSi) was synthesized according to a previous study [3]. Briefly, the synthesized 0.5 g MnSi, 1.25 g PVP (As a porogen for PVDF membranes) and 2.5 g PVDF powders were evenly mixed, completely dissolved in 25 mL DMF solution, vigorously stirred in a 60 °C water bath for 12 h, the polymer was completely dissolved to form a homogeneous solution. After the reaction is over, pour a small amount of casting solution on the glass, scrape the film with a film scraper (thickness 500 μm), and then quickly put it into water to solidify. Finally, the generated PMn membrane was cut into discs with a uniform size and a diameter of 2.5 cm using a puncher, and stored in

43   deionized water before use (**Scheme 1**).
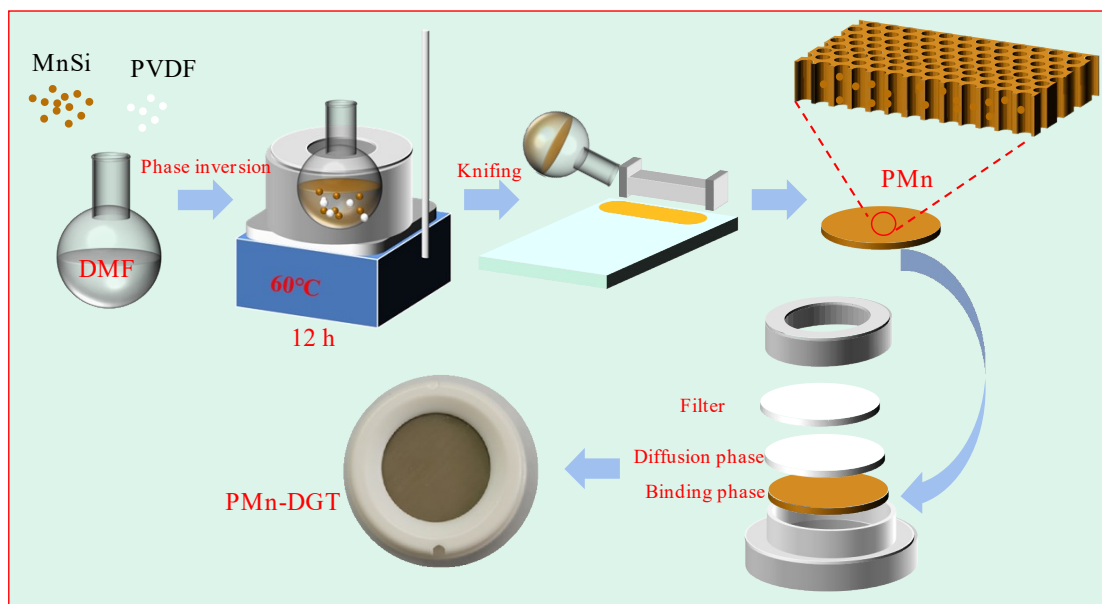
Scheme 1. Flow chart of synthesis and assembly of PMn membrane.

46   **Batch adsorption experiment**

47   The adsorption properties of MnSi to several common heavy metals (Co^{2+}, Ni^{2+},

48   Cd^{2+}, Zn^{2+}, Cu^{2+}, Pb^{2+}) in single and multiple heavy metal systems were discussed by

49   batch adsorption experiments. The initial pH of the solution was adjusted with NaOH

50   or HNO_3. Use a constant temperature shaker to perform constant temperature

51   shaking at 120 r min^{-1} and 25 °C for 12 h. The samples were filtered through a 0.45 μm

52   membrane, and the concentration of heavy metals in the filtrate was determined by

53   Inductively coupled plasma-mass spectrometry (ICP-MS, PerkinElmer NexION 300X).

54   All adsorption experiments were performed at room temperature. All experiments

55   were repeated 3 times. Unless otherwise specified, the initial pH values of the

56   solutions were all neutral. The distribution coefficient (K_d) was calculated using the

57   following equations.

58
$$K_d = \left(\frac{C_0 - C_f}{C_f} \right) \times \frac{V}{m}$$

59   where V is the solution volume of the heavy metals (mL), m is the mass of the

60   adsorbent (g), and C_0 and C_f are the initial and equilibrium solution concentrations of

61   heavy metals (mg L^{-1}), respectively.

62   **Analytical methods**

63   An X-ray diffractometer (Bruker D8 Advance) was used to study the main

64   composition and crystallinity of MnSi. The nitrogen adsorption and desorption

65   instrument (BET: MikeASAP2460) measured the specific surface area and pore size of

66   MnSi. High-resolution transmission electron microscope images (HR-TEM: FEI Tecnai

67   F20) were used to characterize MnSi and observe surface topography and high-

68   resolution images. At the same time, the amorphous structure of the material was

69   identified by combining selected area electron diffraction (SAED). The functional

70   groups on the surface of the material were further tested using Fourier transform

71   infrared spectroscopy (FT-IR: Nexus 670) powder conventional tableting mode.

72   **DGT Analysis Method and Calculation**

73   DGT devices are composed of DGT abrasives, filter membranes, diffused phases,

74   and bound phases [4]. Based on the standard principle of DGT, the concentration of

75   heavy metals detected by PMn-DGT can be calculated according to the Equation (1) [5,

76   6]

$$M = \frac{C_e(V_e + V_g)}{f_e}$$

77   (1)

78   In the formula: C_e is the concentration of heavy metals in the extract, V_e is the

79   volume of the extractant, V_g is the volume of the stationary phase (discs are generally

80 recorded as 0.2 mL), and f_e is the extraction rate of heavy metals.

81   Calculate the DGT concentration using Equation (2)：

$$C_{DGT} = \frac{M\Delta g}{DAt}$$

82   (2)

83   In the formula: M is the cumulative amount of Pb^{2+} in the fixed film (μg), Δg is the

84 thickness of the diffusion layer (cm), D is the diffusion coefficient of Pb^{2+} in the DGT

85 diffusion layer (cm^2 s^{-1}), A is the area (cm^2), t is the placement time of the DGT device

86 (s).

Application of soil

88   To test the monitoring performance of PMn-DGT, the soil to be tested needs to

89 be cultured in advance. The surface polluted soil (0-20 cm depth) was collected from

90 4 points inside and outside a waste lead-acid battery in Chengdu. The pre-cultivated

91 soil was incubated at 25°C for 24 h and used as the soil samples to be monitored by

92 the DGT equipment (n=3). Assemble and deploy the prepared DGT unit according to

93 the instructions, tapping the DGT lightly several times to ensure complete contact

94 between the filter surface of the sampler and the soil. Second, put all the DGTs flat

95 into plastic bags containing a small amount of water to keep the water balance, and

96 incubate at 25°C for 24 h. After the deployment and cultivation are completed, take

97 out the DGT, wash the soil sample adhered to the surface of the DGT with pure water

98 and remove it, carefully take out the DGT binding phase with tweezers, and put it into

99 a 5 mL centrifuge tube. During the whole experiment, 8 treatment groups were set

100 up, and PMn-DGT and commercially available DGT were deployed in 4 soils (the

101 available content of Pb in the 4 soils was different). Each treatment set 3 replicates.

102 The extracted DGT was first eluted with 2 mL of 1 mol L^{-1} HNO$_3$ solution for 2 h to

103 determine the content of Pb enriched in DGT (the selection of elution time and

104 corresponding elution efficiency was determined by the analysis of subsequent

105 experiments). The solution obtained during the experiment passed through a PES

106 syringe filter with a pore size of 0.45 μm, and then the heavy metal content in the

107 sample was analyzed by ICP-MS.

108 **Mechanism for the high selective adsorption of Pb(II) by MnSi.**

109   We carried out a series of comprehensive characterizations of MnSi both pristine

110 and after the reaction. A distinct new peak was observed at approximately 680 cm^{-1}

111 in the Fourier Transform Infrared (FTIR) spectrometer, which can be attributed to the

112 formation of the Pb-O bond (Fig. S6).[7] To further explore the variations of functional

113 groups that occur during the adsorption of Pb^{2+} by MnSi, we employed the two-

114 dimensional correlation FTIR spectroscopy (2D-FITR-COS, Fig. 3a-b). Based on Noda's

115 principle,[8] by carefully analyzing the cross-signal peaks in both the synchronous and

116 asynchronous plots, we were able to elucidate the order of functional group reactions

117 as Si-O-Si > Mn-O > Pb-O > OH. From this result, we hypothesized that there might be

118 a potential ion exchange process between Mn and Pb ions. To verify this speculation,

119 we determined different initial concentrations of Pb^{2+}. The experimental results

120 demonstrated that the dissolution of Mn was positively correlated with the initial

121 concentration of Pb^{2+} (Fig. S7), providing strong evidence that supported our previous

122 hypothesis. Similarly, the two peaks observed at 980/578 and 980/681 correspond to

123 the positive signal region in the asynchronous diagram, indicating the preferential

124 occurrence of the Si-O-Si functional peak (Table S1). As can be seen from Fig. 3c, there

125 was an obvious new diffraction peak around 27.3° after adsorption, which matched

126 the main peak of the standard card $Pb_3Si_2O_7$ (PDF#72-0062), corresponding to the

127 (122) crystal plane. Therefore, it could be speculated that in the system where MnSi

128 adsorbs Pb^{2+}, Pb^{2+} in the solution bonds with O in the silicate radical to form a stable

129 Pb-O bond. It has been reported that the configuration of the complex can be

130 determined by introducing KNO_3 as the supporting electrolyte solution, thereby

131 increasing the ionic strength.[9] The results indicated that the increase in the

132 concentration of KNO_3 in the solution has a relatively limited effect on the adsorption

133 of Pb^{2+} on MnSi (Fig. 3d). This finding suggests that the dominant mechanism of MnSi

134 electrostatic adsorption can be excluded, and the process may involve the formation

135 of inner-sphere complexes of Mn and Pb through covalent or ionic bonding.[9,10]

136 Consequently, amorphous structure, the bonding of Pb with O in silicates, the

137 formation of spherical complexes and ion exchange conjointly promoted the capture
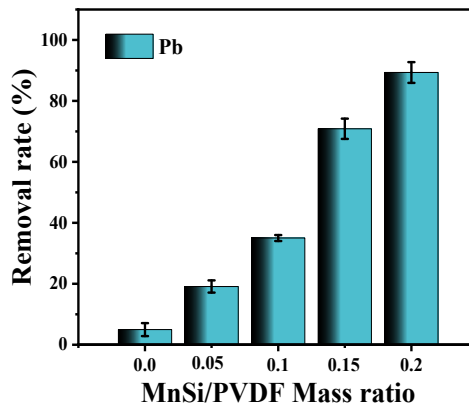
138 of Pb^{2+} by MnSi.

139 **Figures**
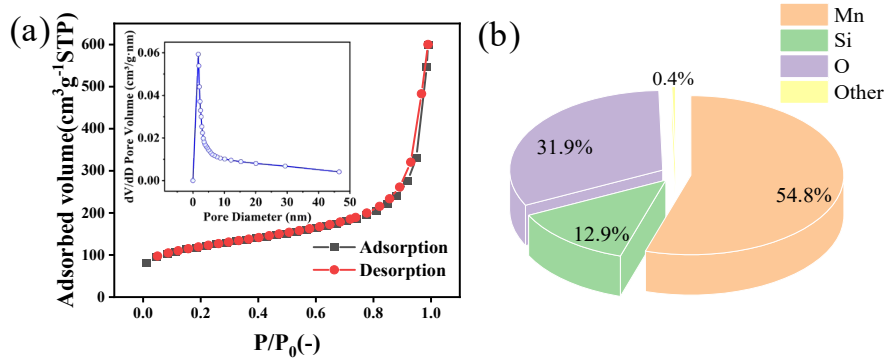
140

141 **Fig. S1** (a) N_2 adsorption and desorption curves and pore size distribution of MnSi; (b)
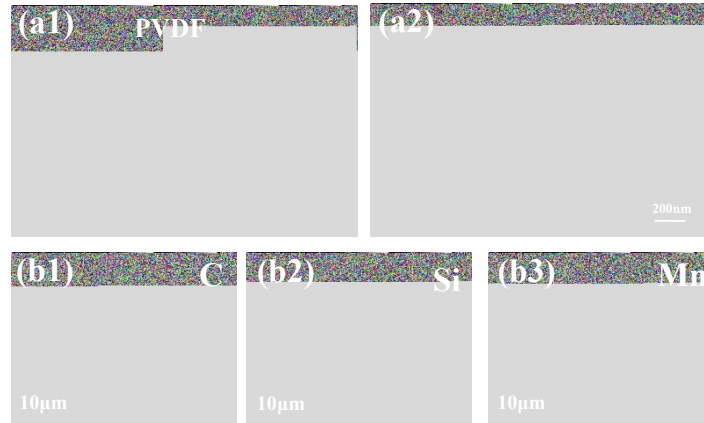
142 The elemental content of MnSi by X-ray fluorescence spectrometer.

143

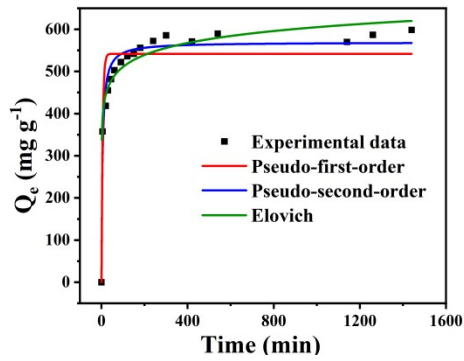144 **Fig. S2** Effect of mass ratio of MnSi/PVDF on adsorption performance of Pb^{2+} by PMn

145 membrane

146

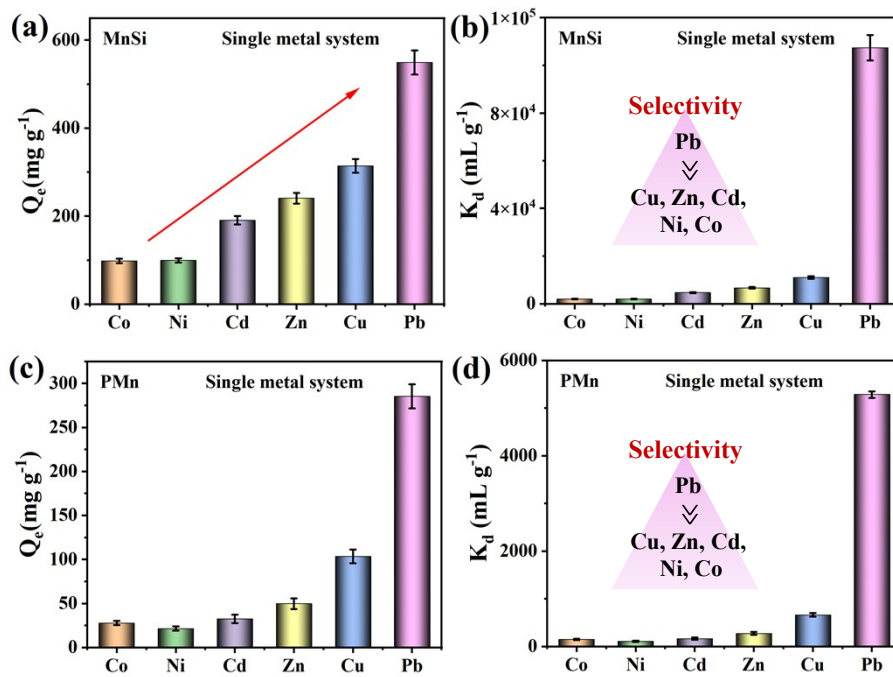**Fig. S3** (a1) Top surface and (a2) cross-sectional SEM images of PVDF membrane. EDS

elemental mapping for (b1) C, (b2) Si, and (b3) Mn of PMn-0.2 membrane.

149

Fig. S4 Adsorption kinetics of Pb^{2+} adsorption by MnSi.

151
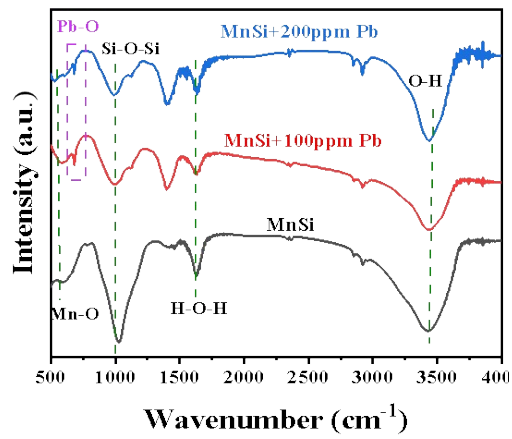
Fig. S5 The selectivity of Pb²⁺ adsorption. (a, c) Adsorption capacity of MnSi and PMn, (b, d) Distribution coefficients K_d of various metals in a single system MnSi and PMn.
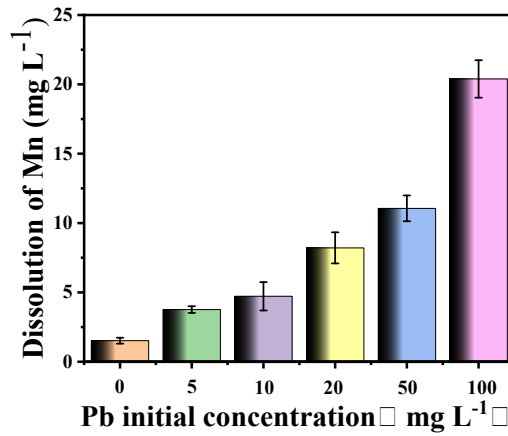
155

156

Fig. S6 FTIR before and after MnSi adsorption.

158

Fig. S7 The effect of the initial concentration of Pb^{2+} on the dissolution of Mn^{2+}.

160
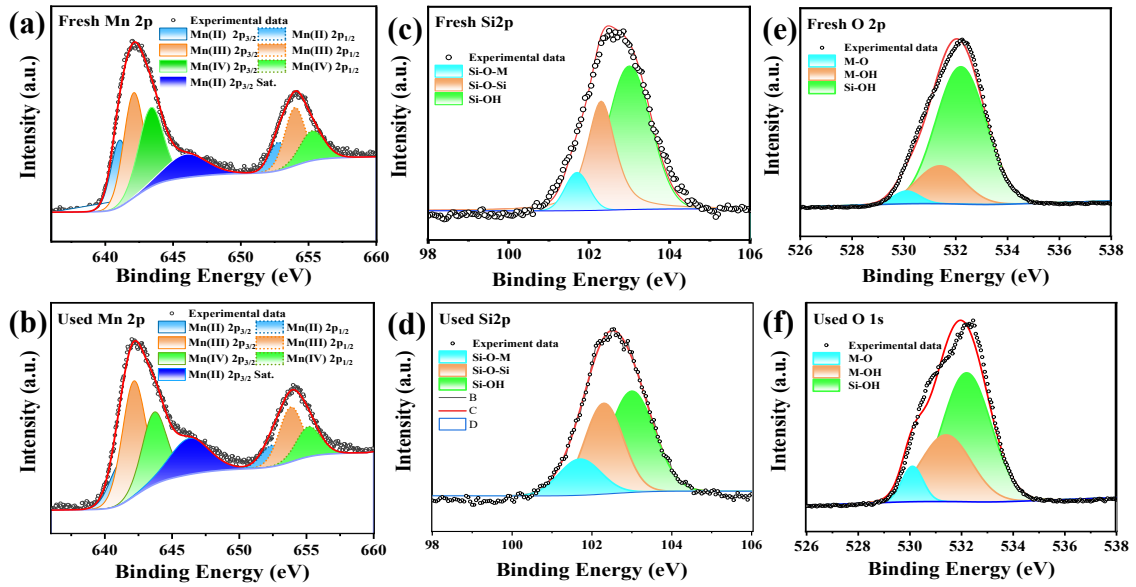
161

162 **Fig. S8** XPS spectrum of the MnSi before and after Pb^{2+} adsorption; (a-b) Mn 2p, (c-d)

163 Si 2p, and (e-f) O 1s.

164

165

166 **Fig. S9** Effect of (a) pH and (b) ionic strength on the performance of PMn-DGT.

167

168 Fig. S10 (a) Dissolved state content in water and (b) extracted state content in DTPA

169 and C_{DGT} content determined by two DGT in four typical soils.

170   Water and Diethylenetriaminepentaacetic acid (DTPA) were utilized to leach to

171 obtain two forms of soil available content, which were defined as effective soluble and
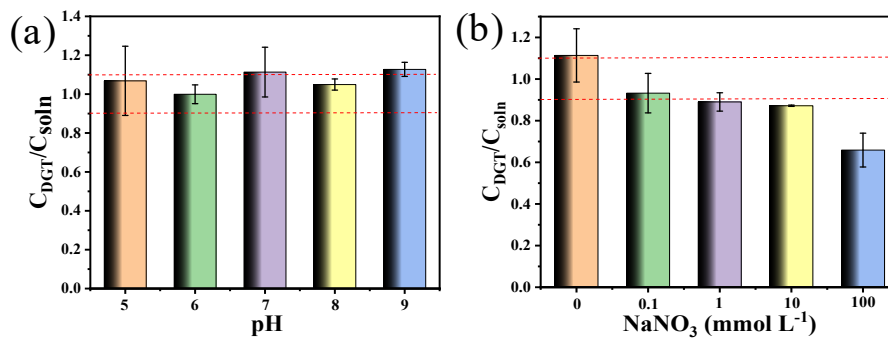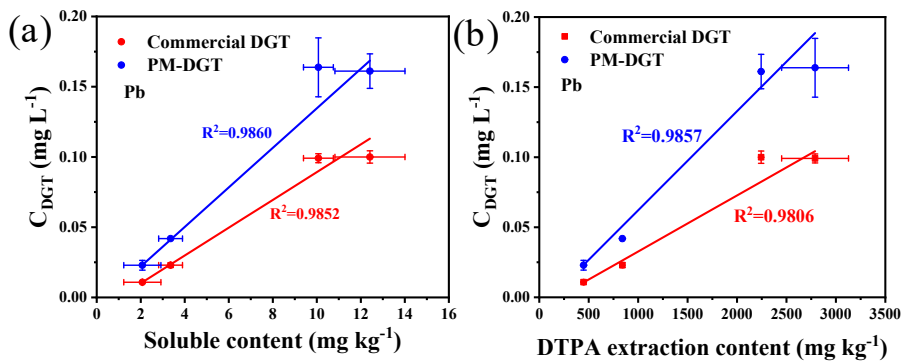
172 DTPA extraction states. A correlation analysis was carried out between the

173 bioavailable Pb content determined by the two methods and the C_{DGT} content

174 measured using DGT, and the results are depicted in Fig. S10. Among the four soil

175 samples, PMn-DGT and commercially available DGT devices exhibited the same trend

176 in the monitoring results of the bioavailable Pb in the soil. Whereas, compared with

177 the concentration measured by the two forms of C_{DGT}, the correlation of PMn-DGT is

178 preferable to that of commercial DGT. Overall, this study aided in unraveling the

179 feasibility of PMn film as a DGT for measuring the effective lead content in soil

180 contaminated by lead-acid battery residues.

181 **Tables**

182 **Table S1** Adsorption kinetics parameters of Pb^{2+} by MnSi.

	Q_e (mg g^{-1})	k_1 (min^{-1})	R^2
Pseudo-first-order	541.9±13.2	0.18±0.04	0.886
	Q_e (mg g^{-1})	k_2 (g (mg min)$^{-1}$)	R^2
Pseudo-second-order	569.2±9.2	3.75E-4± 6.9E-5	0.962
Elovich	α_e (mg (g.min)$^{-1}$)	β_e (g mg^{-1})	R^2
	63.8± 79.7	40.9±3.6	0.975

183   The adsorption kinetic model provides valuable insights into the adsorption

184 mechanism by yielding fundamental parameters (Table S1). The pseudo-first-order

185 and second-order kinetic model fitting parameters are summarized in Table S1.

186 Furthermore, Fig.S4 exhibited the fitting curve of the adsorption amount of MnSi to

187 Pb^{2+} as a function of reaction time. The results demonstrated that during the initial

188 stage, the adsorption of Pb^{2+} increased gradually until reaching the adsorption

189 saturation point, and the adsorption capacity eventually reached as high as 569.2 mg

190 g^{-1}. The fitting performance of the pseudo-second-order model surpasses that of the

191 pseudo-first-order model. In contrast, the pseudo-second-order kinetic model posits

192 that the adsorption rate is predominantly governed by chemical adsorption

193 mechanisms. Consequently, MnSi is a functional adsorbent that can highly adsorb Pb^{2+}

194 and could be an ideal choice for DGT binding phase adsorption materials.

195 **Table S2** MnSi adsorption of different concentrations of Pb^{2+}, MnSi asynchronous

196 images cross peak.

Wavenumber (cm⁻¹)	X-axis / Y-axis	578	681	980	3426
578	Mn-O	+	+(-)	+(+)	+(-)
681	Pb-O		+	+(+)	+(-)
980	Si-O-Si			+	+(-)
3426	O-H				+

197

198 **Table S3** XPS results of the Mn 2p, Si 2p, O 1s for various samples

Element	Name	Peak BE	Fresh-MnSi Atomic %	Used-MnSi Atomic %
Mn 2p	Mn^{2+} 2p3/2	641.0	22.37	17.1
	Mn^{2+} 2p1/2	652.7		
	Mn^{3+} 2p3/2	642.1	40.3	49.84
	Mn^{3+} 2p1/2	653.9		
	Mn^{4+} 2p3/2	643.4	37.33	33.06
	Mn^{4+} 2p1/2	655.3		
	Mn^{2+} 2p3/2 Sat.	645.9		
Si 2p	Si-O-M	101.7	7.89	15.84
	Si-O-Si	102.3	34.29	36.53
	Si-OH	103.0	53.22	47.63
O 1s	M-O	530.1	3.73	7.20
	Mn-OH	531.4	19.82	32.39
	Si-OH	532.2	76.45	60.42

199

200   **Table S4** Physical and chemical properties of the experimental soil.

Index	pH	Organic matter	Available P (mg kg^{-1})	Available K (mg kg^{-1})	Alkali-hydrolyzale N (cmol kg^{-1})
A	8.34±0.07	15.98±1.95	11.81±3.31	134.86±4.62	28.35±4.86
B	8.69±0.02	7.69±1.71	12.26±1.89	172.93±1.11	51.22±4.43
C	8.79±0.01	9.52±1.60	16.50±1.85	186.97±1.15	54.02±2.11
D	8.43±0.01	10.33±1.85	22.24±0.95	160.63±9.08	19.02±1.73

201

202   **Table S5** Contents of common metals in Pb-contaminated soil.

	Fe (g kg^{-1})	Mn (mg kg^{-1})	Cu (mg kg^{-1})	Zn (mg kg^{-1})	Pb (g kg^{-1})	Cd (mg kg^{-1})	Ni (mg kg^{-1})
A	29.0±1.6	438.4±15.3	49.3±5.1	116.1±8.7	0.9±0.09	0.44±0.05	42.2±1.1
B	28.6±1.6	457.8±57.3	49.8±2.6	104.4±2.2	4.0±0.8	0.40±0.05	41.0±2.5
C	27.1±1.4	464.9±28.1	51.1±4.8	102.7±6.1	3.3±0.7	0.38±0.03	34.5±0.6
D	29.7±2.1	575.5±60.8	77.6±11.7	117.7±7.8	15.7±0.1	0.37±0.03	43.3±3.2

203

Table S6 Reagent costs for preparation of MnSi and PMn binding phases (RMB).

Materials	Reagent	Unit price	Specifi cation	Doge	Cost
MnSi（1 g）	$MnCl_2 \cdot 4H_2O$	82.9	500 g	1.9 g	0.37
	$Na_2SiO_3 \cdot 9H_2O$	20	500 g	2.8 g	0.11
Total	0.44				
PMn (Synthesis of 50 pieces)	PVDF	205.9	100 g	2.5 g	5.15
	Polyvinylpyrrolidone	74	100 g	1.25 g	0.92
	N, N-dimethylformamide	18.8	500 ml	25 ml	0.94
	MnSi	0.44	1 g	0.5 g	0.22
Total	7.23 (50 Pieces)				
One piece	0.15				
Chelex (0.3 g cm³) [11]	Chelex-100 resin	2224.7	50 g	0.3 g	13.35
Total	One piece (0.2 cm³) = 2.67				
R-GDC Chelex gel disc	£3.60	About 32 RMB			
R-GDZR Zirconium oxide gel disc	£3.60	About 32 RMB	https://www.dgtresearch.com		

References

1. Ye, J.; Li, C.; Wang, L.; Yan, Y.; Wang, Y.; Dai, J., *Sep. Purif. Technol.,* **2021,** *258*,117669.

2. Yao, Y.; Hu, Y.; Yu, M.; Lian, C.; Gao, M.; Zhang, J.; Li, G.; Wang, S., *Chem. Eng. J.,* **2018,** *344*, 535-544.

3. Cheng, Y.; Zhang, Y.; Wang, Q.; Meng, C., *Colloids Surf., A,* **2019,** *562*, 93-100.

4. Zhang, H.; Davison, W.; Knight, B.; McGrath, S., *Environ.Sci.Technol.,***1998,***32*, (5), 704-710.

5. Ren, S.; Dong, F.; Liu, J.; Bekele, T. G.; Wang, Y.; Zhao, H.; Chen, J.; Tan, F.; Wang, X., *Water Res.,* **2022,** *222*, 118944.

6. Wagner, S.; Santner, J.; Irrgeher, J.; Puschenreiter, M.; Happel, S.; Prohaska, T., *Anal. Chem.,* **2022,** *94*, (16), 6338-6346.

7. Rada, S., Unguresan, M., Zagrai, M., & Popa. Materials, **2022**, 15(22), 8061.

8. He, J., Zheng, H., Ni, F., Shen, F., Xu, M., Tian, D., & Liu, Y. Chem. Eng. J., **2023**, 457, 141195.

9. Yamada N, Katoh M. Chemosphere, **2020**, 249: 126122.

10. Rouff, A. A., Elzinga, E. J., Reeder, R. J., & Fisher, N. S. Environ. Sci. Technol., **2004**, 38(6), 1700-1707.

11. Yuan, Y.; Ding, S.; Wang, Y.; Zhang, L.; Ren, M.; Zhang, C., *Anal. Chim. Acta,* **2018,** *1031*, 98-107.